
Article:

Biskupek, J, Skowron, ST, Stoppiello, CT et al. (9 more authors) (2020) Bond Dissociation and Reactivity of HF and H2O in a Nano Test Tube. ACS Nano, 14 (9). pp. 11178-11189. ISSN 1936-0851

https://doi.org/10.1021/acsnano.0c02661

Bond Dissociation and Reactivity of HF and H_2O in a Nano Test Tube

Johannes Biskupek,[1] Stephen T. Skowron,[2*] Craig T. Stoppiello,[2] Graham A. Rance,[2,3] Shamim Alom,[4] Kayleigh L. Y. Fung,[2] Richard J. Whitby,[4] Malcolm H. Levitt,[4] Quentin Ramasse,[5,6] Ute Kaiser,[1*] Elena Besley,[2] Andrei N. Khlobystov[2*]

[1]Electron Microscopy of Materials Science, Central Facility for Electron Microscopy, Ulm University, Albert-Einstein-Allee 11, Ulm 89081, Germany

[2]School of Chemistry, University of Nottingham, University Park, Nottingham NG7 2RD, United Kingdom

[3]Nanoscale and Microscale Research Centre (nmRC), University of Nottingham, University Park, Nottingham NG7 2RD, United Kingdom

[4]School of Chemistry, University of Southampton, Southampton SO17 1BJ, United Kingdom

[5]SuperSTEM Laboratory, SciTech Daresbury Campus, Keckwick Lane, Daresbury, WA4 4AD, United Kingdom

[6]School of Chemical and Process Engineering and [7]School of Physics, University of Leeds, Leeds LS2 9JT, United Kingdom

*stephen.skowron@nottingham.ac.uk; ute.kaiser@uni-ulm.de; andrei.khlobystov@nottingham.ac.uk

ABSTRACT: Molecular motion and bond dissociation are two of the most fundamental phenomena underpinning properties of molecular materials. We have entrapped HF and H_2O molecules within the fullerene C_{60} cage, encapsulated within a single-walled carbon nanotube $(X@C_{60})@SWNT$ where X = HF or H_2O. $(X@C_{60})@SWNT$ represents a class of molecular nanomaterial composed of a guest within a molecular host within a nanoscale host, enabling investigations of the interactions of isolated single di- or tri-atomic molecules with the electron beam. The use of the electron beam simultaneously as a stimulus of chemical reactions in molecules and as a sub-Å resolution imaging probe allows investigations of the molecular dynamics and reactivity in real time and at the atomic scale, which are probed directly by chromatic and spherical aberration corrected high resolution transmission electron microscopy (Cc/Cs-corrected HRTEM) imaging, or indirectly by vibrational electron energy loss spectroscopy (EELS) *in situ* during scanning transmission electron microscopy (STEM) experiments. Experimental measurements indicate that the electron beam triggers homolytic dissociation of the H-F or H-O bonds, respectively, causing the expulsion of the hydrogen atoms from the fullerene cage, leaving fluorine or oxygen behind. Due to a difference in the mechanisms of penetration through the carbon lattice available for F or O atoms, atomic fluorine inside the fullerene cage appears to be more stable than the atomic oxygen under the same conditions. The use of $(X@C_{60})@SWNT$, where each molecule X is 'packaged' separately from each other, in combination with the electron microscopy methods and density functional theory (DFT) modelling in this work, enable bond dynamics and reactivity of individual atoms to be probed directly at the single-molecule level.

KEYWORDS: endohedral fullerenes; transmission electron microscopy; carbon nanotubes; DFT modelling; single molecule dynamics.

The dynamics of chemical bond dissociation underpin all chemical reactions from simple molecules in the gas phase to complex biochemical processes in living organisms. Recently, transmission electron microscopy (TEM) has emerged as a tool for triggering and imaging bond dissociation in single molecules by harnessing the kinetic energy of fast electrons of the e-beam transferred to atoms of the molecules, whilst imaging transformations induced by the e-beam.[1–5] Within this concept, termed chemical TEM ('ChemTEM'),[1,4] the e-beam acts simultaneously as a source of energy for bond dissociation and a probe used to follow this process at the single-molecule level in a spatiotemporally continuous fashion. The amount of energy transferred from the e-beam to the molecule is well-defined and controlled precisely and, provided that individual molecules are separated from the bulk and entrapped within a protective inert matrix, such that their positions and orientations are controlled, ChemTEM can potentially deliver fundamental information about molecular dynamics.[1,6] In this respect, the ChemTEM approach is akin to matrix isolation spectroscopy, except that the molecules are trapped in an inert solid matrix at room temperature, with the e-beam acting as both a pump (kinetic energy transfer) and a probe (imaging / local spectra). A single-walled carbon nanotube is the most robust and effective matrix for molecular encapsulation for experiments in TEM. It can also restrict the molecular motion by confining the guest-molecules within the nanoscale channel and as such can be viewed as a tiny test tube[7–12] or a one-dimensional support for adsorbed molecules as demonstrated more recently.[13–15] Possessing a superior mechanical strength and outstanding electrical and thermal conductivities, this nano-test-tube can effectively protect the guest molecules from the possible detrimental effects of the environment during TEM measurements, such as heating, ionisation or chemical etching.[1,16] Using this approach, we have previously investigated the energetics and dynamics of several heteroatomic bonds, including C-H, C-D, C-S, C-Cl, Mo-I, and Re-Re at the single-molecule level.[1,3,5,17,18] A similar approach has been applied for studying reactions of fullerenes triggered by C-C bond dissociation.[19,20] However, until now, this approach was not applicable to small volatile molecules, such as water, because of the vacuum conditions in TEM, while the fast molecular motion of such small molecules also seemed to prohibit any ChemTEM investigation at the single-molecule level.

Fullerene C_{60}, with a cavity analogous to a very small nanotube, provides an ideal platform for the entrapment of isolated atoms or di- and triatomic molecules, such as H_2, HF and H_2O.[21–27] Vibrational, rotational and magnetic analysis of isolated small molecules entrapped in C_{60} showed that their behaviour is much closer to the gas phase than the liquid, thus allowing investigations of the fundamental properties of isolated molecules unperturbed by strong intermolecular forces. In this study, we inserted hydrogen fluoride and water molecules pre-packaged in fullerene cages, $HF@C_{60}$ and $H_2O@C_{60}$, into a single-walled carbon nanotube (SWNT), leading to chains of endohedral fullerenes inside SWNT denoted as $(HF@C_{60})@SWNT$ and $(H_2O@C_{60})@SWNT$, respectively. This geometry allowed us to probe the bond dissociation in HF and H_2O under the electron beam and to image and follow this process in individual fullerene molecules.

The paper is structured as follows: (1) HRTEM imaging of fullerenes, their stability with different encapsulated species, and stability at different beam energies; (2) HRTEM imaging of endohedral species, analysis of transient F/O atom contrast, and HRTEM image simulations; (3) STEM imaging, STEM-EELS spectroscopy of single F atoms, and aloof-mode vibrational EELS of endohedral fullerene nano-sheets; (4) consideration of the energy transfer from the e-beam, and the available mechanisms of bond dissociation; and (5) computational modelling of bond dissociation, DFT-MD of atom emission processes and energetic hydrogen atoms, and transition state analyses for emission of F and O atoms.

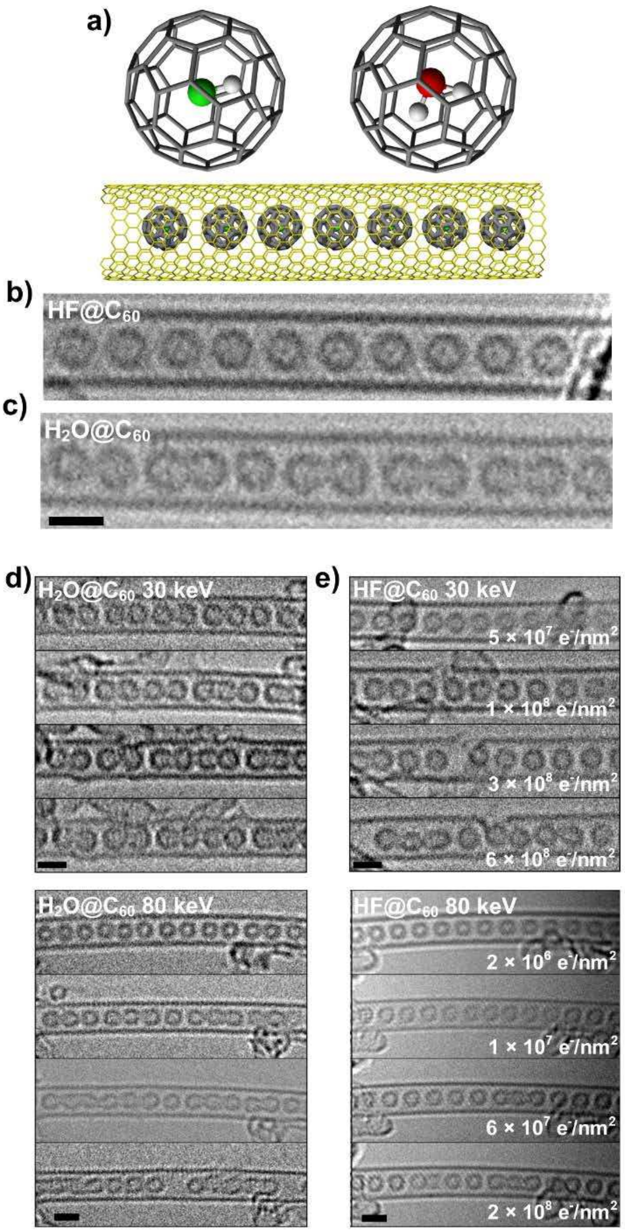

Figure 1. (a) Structural diagrams of HF@C_{60}, H_2O@C_{60} and endohedral fullerenes in a carbon nanotube. 30 keV chromatic and spherical aberration (Cc/Cs) corrected HRTEM images of (b) (HF@C_{60})@SWNT and (c) (H_2O@C_{60})@SWNT at ~5 × 10^7 e^- nm^{-2}. (d, e) Comparison of HF@C_{60} and H_2O@C_{60} transformations at 30 keV and 80 keV electron irradiation: at 30 keV images of H_2O@C_{60} show signs of decomposition after a dose of 10^8 e^- nm^{-2} manifesting through the oligomerisation of the fullerenes, whilst images of HF@C_{60} indicate that the fullerene cages are more stable even for larger doses of electrons. At 80 keV both endohedral fullerenes exhibit much higher reactivity (~10 more reactive). The total electron dose accumulated by the sample is shown, rather than time, because the electron dose is relevant to the progression of reactions under the electron beam in ChemTEM. (The time series are also included as Supporting Videos 1-4). All scale bars are 1 nm.

RESULTS AND DISCUSSION

We have encapsulated HF and H_2O molecules inside C_{60} by a previously reported method of 'molecular surgery', involving the insertion of the guest molecules into an open fullerene cage followed by the reconstruction of the C_{60} cage *via* a series of chemical transformations as described in references 26 and 28, respectively (Fig 1a). This synthetic approach followed by HPLC purification yields HF@C_{60} and H_2O@C_{60} materials of 99% purity where virtually every fullerene molecule contains a molecular guest. The two endohedral fullerenes have been inserted separately into open SWNT with an average diameter of ~1.4 nm by evaporating the molecules in vacuum in the presence of nanotubes. Each endohedral fullerene molecule appears to fill the SWNTs as efficiently as pure (empty) C_{60}, filling the entire nanotube length without gaps, to form two materials: (HF@C_{60})@SWNT and (H_2O@C_{60})@SWNT. This process is driven by strong dispersion interactions that are maximised by the ideal match of the fullerene diameter (0.7 nm) with the diameter of the nanotube (~1.4 nm).[16,29]

HRTEM imaging of fullerene cages. TEM imaging of (HF@C_{60})@SWNT and (H_2O@C_{60})@SWNT materials reveals ordered chains of fullerene molecules that appear as circles separated by van der Waals gaps of ~0.3-0.4 nm, within the cylindrical channel of the nanotube (Fig 1b), very similar to the empty C_{60} in nanotubes reported in many previous studies (for example reference 30). However, unlike the empty C_{60} fullerenes that exhibit no observable damage even at higher e-beam energies such as 40 keV,[30] the endohedral fullerene molecules undergo noticeable cross-linking and polymerisation under the 30 keV e-beam irradiation (Fig 1c,d,e). TEM imaging indicates a greater stability of HF@C_{60} than H_2O@C_{60} (Supporting Information S9), as the images of the former molecules remain unchanged up to applied electron doses of more than $2{\cdot}10^9$ e^- nm^{-2} (this dose corresponds to about 1000 single HRTEM images in the conditions used for these experiments). This equates to a factor of 6.8 times higher stability of HF@C_{60} than H_2O@C_{60} at 30 keV. With increasing energy of the e-beam from 30 keV to 80 keV, the stability of both endohedral fullerenes drastically decreases by a factor of 10.7 for HF@C_{60} and 8.0 for H_2O@C_{60}, providing a useful insight into the mechanisms of e-beam damage as discussed later.

HRTEM imaging of endohedral HF and H_2O. We observed contrast consistent with that of a single-atom of F or O at the centre of the molecule (Fig 1b), which is completely absent in empty fullerene cages in C_{60}@SWNT under the same conditions, consistent with previous works, for example reference 31 (Supporting Information S1 and Supporting Video 5). While the endohedral HF is known to be present in virtually all the molecules as evidenced by HPLC and mass spectrometry analysis,[28] HRTEM contrast of fluorine in (HF@C_{60})@SWNT can be visually identified in about 35% of all the molecular images we analysed at 30 keV (based on the observation of 468 molecular frames), which decreases to ~10% of molecular images at 80 keV (Supporting Videos 1 and 3). The higher stability of the molecules in ($HF@C_{60}$)@SWNT allowed us to analyse the single-atom contrast dynamics within the same molecule over time, by taking time series of images. The contrast associated with the F atom appears to be transient within the same molecule emerging and vanishing at different times (Fig 2a,b; Supporting Information S2, showing an extracted still from Supporting Video 1). Single-atom contrast of O atoms in ($H_2O@C_{60}$)@SWNT is significantly more difficult to detect, only observable in ~10% of the molecular images analysed at 30 keV (997 molecular frames), and becoming undetectable at 80 keV due to the fast onset of the fullerene cage damage (Fig 2d,e; Supporting Videos 2 and 4).

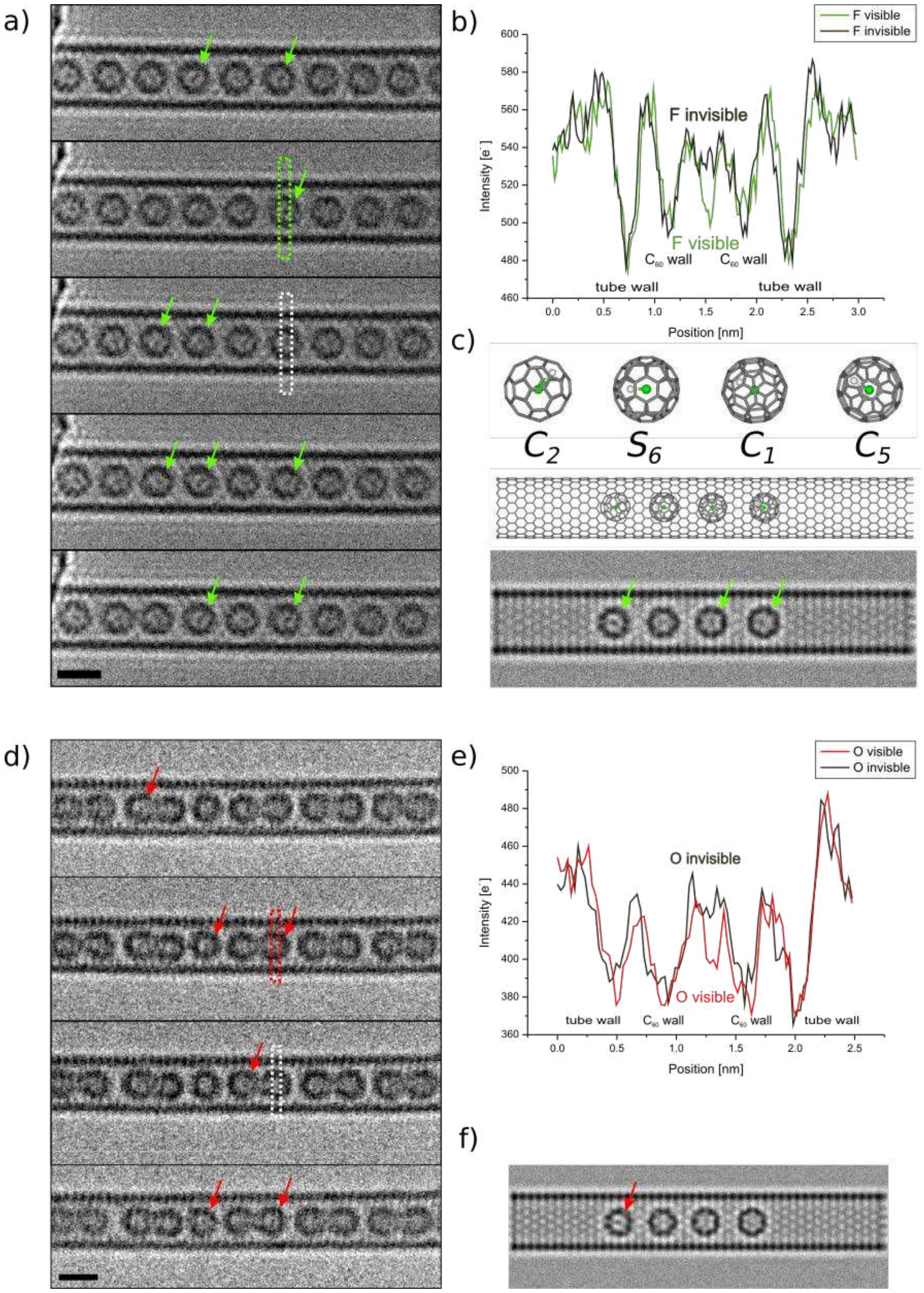

Figure 2. (a) Experimental time series (2 s time interval) of 30 keV Cc/Cs-corrected HRTEM images of $(HF@C_{60})@SWNT$, showing blinking of the F-atoms. The green arrows indicate examples when the F-atoms are clearly visible, these appear to be visible and invisible in the same molecules over time (see Supporting Video 1). (b) Line profile across the centre of a fullerene molecule (as shown in green and white boxes indicated in micrographs (a)) showing variation of image contrast when F-atom is visible (green plot) or invisible (black plot) within the same molecule. (c) Model and corresponding HRTEM image simulations for four different orientations of $HF@C_{60}$ in SWNT (four principal projections along elements of symmetry of the C_{60} cage C_2, S_6, C_1 and C_5). Only some orientations are able to produce a ‘dot’ contrast at the centre of the fullerene cage due to an overlap of F-atom with two C-atoms of C_{60}, indicated with green arrows. A neutral

atom of fluorine in the cage $F^0@C_{60}$ produces contrast in the simulated images that is similar to the experimental images (see Supporting Information S7). (d) Time series (~2 s time interval) of 30 keV Cc/Cs-corrected HRTEM images of $(H_2O@C_{60})@SWNT$ showing blinking of the O-atoms. The red arrows indicate examples when the O-atoms are visible (see Supporting Video 2). (e) Line profile across the centre of a fullerene molecule (as shown in red and white boxes indicated in micrographs (a)) showing variation of image contrast when O-atom is visible (red plot) or invisible (black plot) within the same molecule. Note that observation of a single O-atom is more challenging and less distinct than F-atom due to the lower Z-number of oxygen and lower stability of $H_2O@C_{60}$ under the electron beam. (f) Simulated HRTEM image of $H_2O@C_{60}$ in SWNT showing that single O-atom contrast is observable only in some orientations (see Supporting Information S8). All scale bars are 1 nm.

We modelled the positions and orientations of the $F@C_{60}$ in nanotube and simulated HRTEM images and STEM images, which demonstrate that the contrast at the centre of $F@C_{60}$ can emerge only for certain orientations of the molecule, namely projections along the C_2 and C_1 symmetry axis of the fullerene cage (with two carbon atoms at the centre directly on top of each other, Fig 2c). In this configuration, two carbon atoms of the C_{60} cage overlap with the F atom such that a column of three atoms produces sufficient contrast, consistent with experimental HRTEM images. Other orientations, such as projections along S_6, do not produce such contrast. Furthermore, the observed transient nature of the F atom contrast in $F@C_{60}$ suggests a homolytic dissociation pathway of HF under the e-beam, as also predicted by our theoretical calculations below. HRTEM image simulations performed for the models with neutral, positive or negative F-atom within C_{60} reveal that only in the case of the charge-neutral fluorine $F^0@C_{60}$ (or $HF@C_{60}$) can the transient contrast at the centre of fullerene be observed (Supporting Information S7). In the case of the $F^-@C_{60}$ or $F^+@C_{60}$ the contrast is permanently absent or permanently present respectively, which would disagree with our experimental observations (changes in electron charge density around the atom affect the core potentials, hence a spatially extended signal in the projected potential and the observed single-atom contrast in HRTEM, as described in reference [32]; Supporting Information S7). Similar HRTEM image simulations of $H_2O@C_{60}$ show that the central atom contrast is weaker and observable for even fewer orientations of the molecule (Fig 2f), consistent with our experimental HRTEM observations. The implications of the transient atom contrast regarding rotation of the fullerenes are discussed in Supporting Information S10.

STEM imaging and EEL spectroscopy. In order to further elucidate the behaviour of $HF@C_{60}$ under the electron beam, $(HF@C_{60})@SWNT$ and a $HF@C_{60}$ nano-sheet were analysed by scanning transmission electron microscopy (STEM) at 60 keV (Fig 3a-d). High angle annular dark field (HAADF) imaging also indicated the presence of additional contrast at the centre of the C_{60} cage (Fig 3a), corresponding to the likely position of the F atom. The images are intrinsically noisier than the HRTEM images shown in Fig 1 due to unavoidable noise in the STEM-HAADF mode at these low electron dose-rates (Fig 3b, see Methods for further details on the simulations). Similar to HRTEM, with continued irradiation at a dose rate of $1.4 \cdot 10^{7}$ e^{-} nm^{-2} s^{-1}, the C_{60} fullerenes visibly change shape and undergo cross-linking and oligomerisation, with four of the individual fullerenes initially observed in Fig 3a fully cross-linked after a total electron dose on the molecules of $5.5 \cdot 10^{8}$ e^{-} nm^{-2} (dose impinging on the molecules estimated between the first recorded image of these molecules and the acquisition of the image shown in Fig 3c).

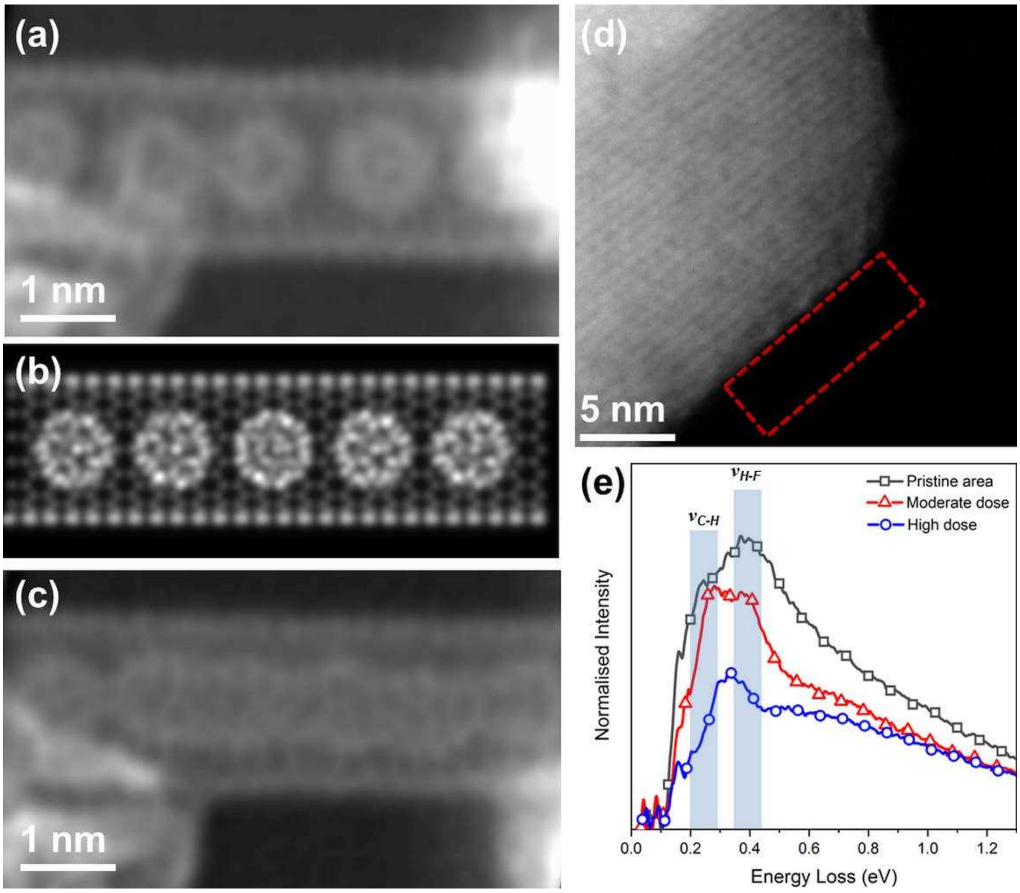

Figure 3. 60 keV Cs-corrected high-angle annular dark-field scanning transmission electron microscopy (C_S-corrected HAADF STEM) imaging of (a) (HF@C_{60})@SWNT and (d) HF@C_{60}. The type of contrast due to the F atom in the centre of the fullerene cage in (a) is commensurate with that expected from STEM image simulations (b). Extended exposure of (HF@C_{60})@SWNT to the e-beam results in the oligomerisation of the fullerene cages (c). (d) C_S-corrected HAADF-STEM image of HF@C_{60} nano-sheet; a typical region for recording aloof vibrational spectra is illustrated by the dashed red box. (e) Vibrational EELS recorded in aloof configuration near the HF@C_{60} nano-sheet (black) indicates the presence of a strong band at 0.38 eV which corresponds to the H-F stretching vibration mode which decreases in intensity (red and blue) as the nano-sheet is

irradiated extensively, providing evidence for the cleavage of the H-F bond. A peak at 0.28 eV, consistent with a C-H stretching band, is the main feature of the EELS after moderate e-beam irradiation.

In addition to e-beam damage to the host C_{60} molecules allowing the endohedral F to move more freely, the low inelastic scattering cross-section of F at its K ionisation edge makes the spectroscopic identification of single F atoms challenging: Fig. 4 nevertheless presents strong evidence of the presence of single F atoms in two intact C_{60} molecules, whereas no F signal is detected within polymerised molecules (see methods for experimental details). Vibrational electron energy loss spectroscopy (EELS) performed on the molecules in individual nanotubes did not show sufficiently strong signal from the endohedral molecules due to the large amount of carbon around them (relative to the small molecule concentration) and to possible screening effects of the host nanotube; however EELS of a nano-sheet of HF@C_{60} approximately five monolayers thick and suspended over a hole (Fig. 3d) in an aloof beam configuration to protect the molecules from the impact of the e-beam itself,[31,33–35] revealed strong vibrational features in the region between 0.1–1.7 eV (~800-13700 cm^{-1}). The observed vibrational bands before and after intentional e-beam irradiation are compared in Fig. 3e. The initial spectrum is dominated by a band at 0.38 eV (~3000-3100 cm^{-1}), corresponding to the H-F stretching vibration mode,[26] that decreases in intensity after moderate e-beam irradiation of an estimated total dose of $2.0 \cdot 10^{6}$ e^{-} nm^{-2} (dose rate of $8.0 \cdot 10^{3}$ e^{-} nm^{-2} s^{-1}). After the moderate irradiation the spectrum becomes dominated by a band at 0.28 eV (~2200-2300 cm^{-1}) which is consistent with the C-H stretching vibration mode. After significant further irradiation of a total dose of $1.9 \cdot 10^{7}$ e^{-} nm^{-2} (dose rate of $2.5 \cdot 10^{5}$ e^{-} nm^{-2} s^{-1}) both bands significantly diminish, leaving a much weaker band at 0.33 eV (~2600-2700 cm^{-1}) remaining as background (Fig. 3e). Energy-dispersive X-ray spectroscopy (EDX) of HF@C_{60} crystals in TEM at 80 keV shows the continued presence of a virtually unchanged fluorine signal after irradiation at higher total doses than this, demonstrating that while the H-F bonds break under the e-beam fluorine atoms persist in the fullerene cages.

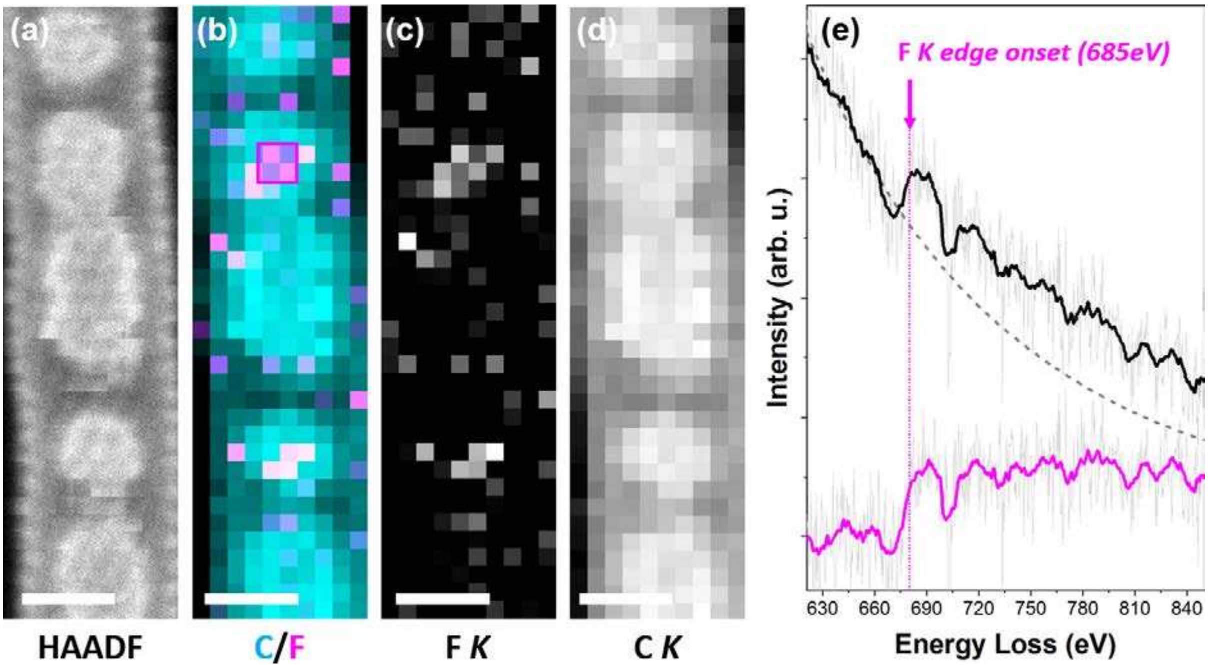

Figure 4. 60 keV electron energy loss spectroscopy (EELS) fingerprinting of F single atoms in the $(HF@C_{60})@SWNT$ system. (a) HAADF contrast acquired simultaneously with the EELS signal, showing a number of intact and polymerised C_{60} host molecules within a SWCNT. (b) False-coloured composite map showing a clear increase of F signal (magenta) within two of the intact C_{60} molecules (C is displayed in cyan). This composite map was created from the chemical maps generated by integrating the intensity of the F *K* (c) and C *K* (d) ionisation edges at each pixel of the spectrum image. (e) Experimental single spectrum at the F *K* ionisation edge averaged over the neighbouring pixels highlighted by the magenta box in (b). Smoothed data (solid lines) are overlaid on top of the unprocessed raw spectra (light grey line) before (black) and after (magenta) background subtraction using a power law model (dashed grey line). The onset of the F K edge (table value at 685 eV, dashed magenta line) is clearly visible.

Energy transfer and bond dissociation under the electron beam. The diatomic HF and triatomic H_2O molecules entrapped in $HF@C_{60}$ and $H_2O@C_{60}$, respectively, such that the F atom and O atom are positioned at the centre of the icosahedral C_{60} cage, retain all three rotational degrees of freedom for the HF and H_2O, but little translational freedom, limited to ~0.2 nm by the fullerene cage.[21–27] The guest molecules are tightly packed in a SWNT, such that at room temperature HF and H_2O molecules entrapped inside the fullerene, and the fullerene cage entrapped in the nanotube (the rotation activation barrier is as low as 0.008 eV for fullerene nanotube $C_{60}@SWNT$ at room temperature[36]) both have unrestricted rotational freedom. Therefore, in their pristine state, the $(HF@C_{60})@SWNT$ and $(H_2O@C_{60})@SWNT$ systems can be described as consisting of a free-rotator within a free-rotator. A recent theoretical study exploring a hypothetical $(HF@C_{60})@SWNT$ structure concluded that HF molecules in neighbouring $HF@C_{60}$ are expected to interact by dipole-dipole coupling of the order of only several meV.[37] Overall, the state of entrapped molecules in $(HF@C_{60})@SWNT$ and $(H_2O@C_{60})@SWNT$ is thus closer to the gas state in terms of rotation and vibration, but in terms of translation it is closer to a solid crystalline state, such that the lateral positions of individual molecules during TEM imaging are severely constrained. The calculations described below (see Methods) show that the geometry of entrapped small molecules is almost identical to the gas phase (see Supporting Information S4).

In order to explain our TEM observations of ($HF@C_{60}$)@SWNT and ($H_2O@C_{60}$)@SWNT, we must consider what happens to these molecules under the e-beam. The extremely short pathway of the e-beam within these materials due to their thickness of only ~2 nm eliminates most secondary damage processes, while the SWNT acts as an efficient sink of heat and charge; the effects of most typical damage mechanisms under the e-beam are removed.[38] In addition to this stabilising effect observed in our previous studies,[1] the direct encapsulation of each individual molecule in a fullerene separates them from one another by a distance of 1 nm. The reactive molecules - including any activated species created by the beam - are protected from contact with neighbouring molecules by the unreactive interior of C_{60}, such that the fundamental properties of individual molecules can be studied. While the fullerene remains intact, permanent structural change to the molecules requires the ejection of atoms through the fullerene cage, which can only plausibly occur *via* a direct knock-on (DKO) collision imparting a large kinetic energy to an atom. Any other process of bond scission such as radiolysis will be quickly reversed, due to the confinement of the molecular atoms in close proximity to one another within the volume of the cage. The observed drastic decrease of stability by a factor of 10.7 for $HF@C_{60}$ and 8.0 for $H_2O@C_{60}$ as the energy of the e-beam is increased from 30 keV to 80 keV (in otherwise identical experimental conditions), confirms that the DKO is the main driving force of molecular transformations under our conditions (the opposite would be true for any effects induced by electron-electron collisions, such as radiolysis).

In a DKO collision, the maximum amount of energy transferred from the incident electron E_{Tmax} is directly proportional to the kinetic energy of that electron E and inversely proportional to the mass of the stationary atom M with which the electron collides[6] (the process shown in Fig. 5e):

$$E_{Tmax} = \frac{2ME\left(E+2m_ec^2\right)}{(M+m_e)^2c^2+2ME} \qquad \text{(equation 1)}$$

m_e is the electron mass. In ($HF@C_{60}$)@SWNT and ($H_2O@C_{60}$)@SWNT the atom that can receive the largest amount of kinetic energy is hydrogen – the lightest atom. The maximum amount of energy transferred to the H-atom from the 30 keV e-beam (E_{Tmax}^{H}) is 67.8 eV (equation 1) which exceeds the energy barrier for dissociation of the F-H or O-H bonds by an order of magnitude (Fig. 5a,b).

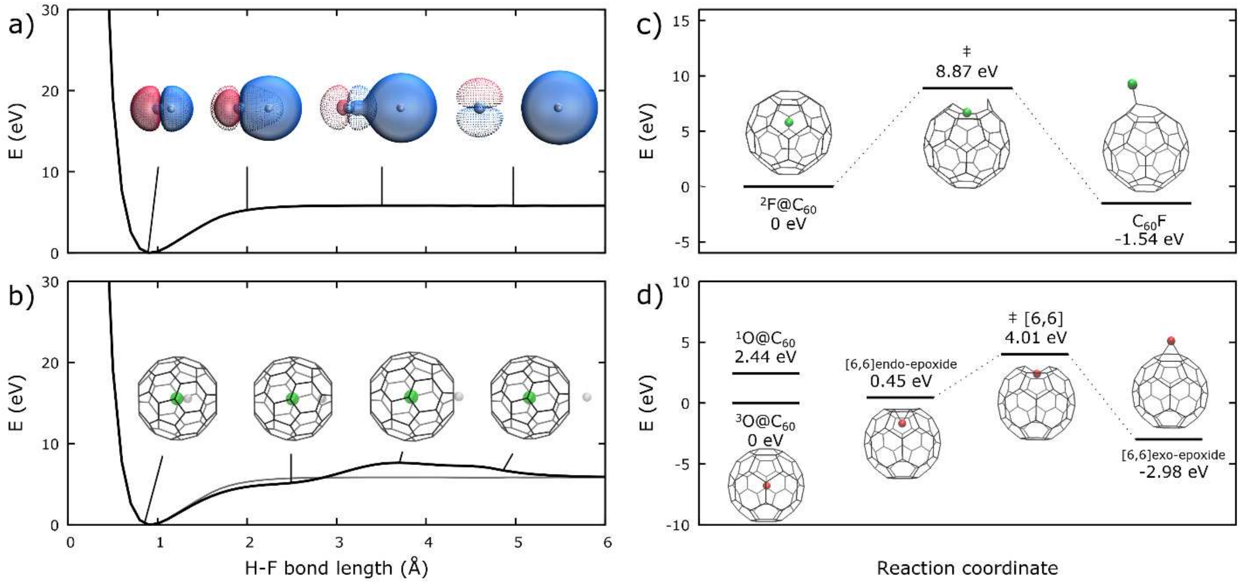

e) Direct energy transfer (as in equation 1)

$$e^- \longrightarrow X$$

$$E \longrightarrow E_{Tmax}^{X}$$

f) Energy transfer via hydrogen (as in equation 2)

$$e^- \longrightarrow H \longrightarrow X$$

$$E \longrightarrow E_{Tmax}^{H} \longrightarrow E_{Tmax}^{X\prime}$$

Figure 5. (a) The ground state energy profile of homolytic HF dissociation (each atom retains one valence electron from the covalent bond and remains charge neutral), showing the spatial extent of the alpha (dotted) and beta (solid) electrons in the relevant orbital at increasing interatomic distance (see Supporting Video 6 for an animation of this process). (b) The effect of the fullerene cage on the shape of this energy profile, showing ejection of hydrogen from $HF@C_{60}$ through the centre of a hexagonal face of the cage; the thin grey line indicates the potential shown in (a) with the energy shifted so that both ground state energies are zero. The initial barrier to dissociation is slightly lowered, but transmission through the fullerene wall adds an additional barrier at increased bond length and introduces a barrier to recombination of HF once the hydrogen atom is ejected from the fullerene cage. Transition states and associated energies for the key steps in ejection of (c) fluorine and (d) oxygen atoms through the fullerene cage, showing the relative lability of forming the exohedral epoxide fullerene species $C_{60}O$ compared to the exohedral $C_{60}F$. The latter shows the pathway that is visible to the electron beam, in which the endohedral to exoohedral epoxide bond inversion takes place through a [6,6] carbon-carbon bond (see Supporting Information S5 for more details). A comparison of the maximum energy transfer from incident electrons to atoms *via* direct knock-on collisions, (e) directly to atom X (X = F or O), or (f) *via* an intermediate collision with a hydrogen atom. With an incident electron energy of 30 keV, for fluorine $E_{Tmax}^{F\prime} \approx 3.4E_{Tmax}^{F}$, and for oxygen $E_{Tmax}^{O\prime} \approx 3.8E_{Tmax}^{O}$.

Theoretical modelling of bond dissociation and atom permeation through C_{60}. Our molecular dynamics simulations (described in the methods section) show that at the maximum transferable energy of 67.8 eV, following dissociation from the molecule, the kinetic energy of hydrogen atom is sufficient to continue its movement across the C_{60} cavity and through the fullerene wall, preventing recombination to $HF@C_{60}$ (as shown in

Supporting Video 7). At lower transferred energies, the penetration barrier is dependent on the orientation of the H-atom momentum with respect to the carbon-carbon bonds of C_{60}, while dissociation with kinetic energies insufficient to emit the hydrogen atom from the fullerene cage results in recombination of the parent molecule, reforming the original HF or H_2O structure. These results are consistent with the energy barrier for penetration of a hydrogen atom though the fullerene wall, in the region of 2.6 eV through a hexagon of C_{60}.[39] The minimum threshold energy required for an electron impact to break the H-F bond and subsequently emit the hydrogen from the fullerene is 7.75 eV, which can be compared to the 7.63 eV stationary barrier (Fig 5b). This corresponds to a characteristic electron dose of $7 \cdot 10^7$ e^- nm^{-2} for a single fullerene layer at 30 keV (see Supporting Information S6 for further details). Therefore, under TEM imaging conditions, both HF and H_2O are effectively stripped of hydrogen atoms.

Removal of hydrogen under the electron beam would be expected to result in the homolytic dissociation of the H-F and H-O bonds, such that each atom receives one of the bonding electrons, and becomes a charge neutral radical species. For dissociation of HF, this configuration is 11.8 eV lower in energy relative to the alternative heterolytic pathway resulting in separated H^+ and F^- ions (according to our DFT calculations, see Methods). This is comparable to the 10.2 eV difference between the ionisation energy of hydrogen (13.6 eV) and the electron affinity of fluorine (3.4 eV),[40] and indicates that formation of F^0@C_{60} is highly energetically favourable upon removal of hydrogen, consistent with our TEM observations and image simulations as discussed above. For the dissociation of an isolated water molecule, homolysis is even more preferable than heterolysis: removal of the first hydrogen atom to form hydrogen ($H^{\cdot}$) and hydroxyl ($HO^{\cdot}$) radicals is 13.4 eV lower in energy than forming a proton (H^+) and a hydroxide ion (OH^-). Continuing with the removal of the second hydrogen is 25.8 eV lower in energy when forming another hydrogen radical and a charge-neutral atomic oxygen (O) *via* homolysis compared to a proton and an oxide dianion (O^{2-}) *via* heterolysis. Atomic oxygen has two unpaired electrons as well as a high affinity for bonding with carbon, and is reactive enough with the C_{60} cage to form an endohedral epoxide group. In contrast, the F atom, with a single unpaired electron, cannot engage in stable bonding with the inside of the C_{60} cage and adopts an off-centre position in the cage.

Under the 30 keV e-beam, the carbon atoms of C_{60} receive up to $E_{Tmax}^{C} = 5.6eV$, which is significantly below the barrier for displacement of a carbon atom from fullerenes or nanotubes, suggesting that the C_{60} cage should remain intact under our TEM observation conditions. However, damage of C_{60} cages is apparent in time series images, particularly in the case of (H_2O@C_{60})@SWNT (Fig 1d). Although the 30 keV e-beam can transfer energy to oxygen ($E_{Tmax}^{O} = 4.2eV$) and fluorine ($E_{Tmax}^{F} = 3.6eV$) atoms, our calculations indicate that in both cases the direct impact of the e-beam causes a displacement of the atom from their equilibrium geometries, but is insufficient to emit either atom from the fullerene and initiate the observed damage. In order to explain the behaviour witnessed under the e-beam, it is important to consider the highly energetic hydrogen atoms (up to 67.8 eV of kinetic energy under the 30 keV e-beam) that are generated during the electron irradiation of both HF@C_{60} and H_2O@C_{60}, and the effect they can have on the surrounding atoms. The maximum energy transferred from the e-beam to an atom X is increased if this occurs *via* a collision with a hydrogen atom (the process shown in Fig 5f):

$$E_{Tmax}^{X\prime} = E_{Tmax}^{H}\frac{4M_H M_X}{(M_H+M_X)^2} = \frac{2M_H E\left(E+2m_e c^2\right)}{(M_H+m_e)^2c^2+2M_H E}\frac{4M_H M_X}{(M_H+M_X)^2} \quad \text{(equation 2)}$$

such that the hydrogen atom effectively amplifies the maximum energy transferred from the e-beam to the atom by a factor of ~3.4-3.8 in our conditions. This is due to the low mass of hydrogen being more commensurate with the extremely low mass of the electron, enabling a more efficient transfer of energy than with a direct collision between electron and a heavier atom. Although our simulations of electron impacts on oxygen and fluorine show that neither can receive enough energy from the 30 keV beam directly to penetrate the fullerene cage (E_{Tmax}), in the case of an epoxide oxygen atom a collision with an energetic hydrogen atom can transfer enough energy ($E_{Tmax}^{O\prime} = 15eV$; equation 2) to overcome the 12.7 eV barrier to inversion through the cage (see Supporting Video 8), while this is not the case with F@C_{60} ($E_{Tmax}^{F\prime} = 12.9eV$). The initial H_2O@C_{60} molecule also contains double the amount of hydrogen compared to HF@C_{60}, which increases the likelihood of energy transfer from e-beam *via* an H atom to the O atom. Although the electron beam cannot break bonds of the fullerene cages directly ($E_{Tmax}^{C} = 5.6eV$), our simulations show that the $E_{Tmax}^{C\prime} = 18.9eV$ transferrable from the 30 keV e-beam *via* hydrogen to a carbon atom is also sufficient to create defects in the fullerene structure, explaining why fullerene cages in HF@C_{60} eventually undergo damage and polymerisation at extreme doses even at 30 keV (Fig 1e).

A comparison of the pathways available for the emission of the O and F atoms from inside C_{60} *via* a transition state analysis (Fig 5c,d) is also instructive in this context, although it should be stressed that the e-beam induced reactions (unlike thermally activated ones) do not follow these exact reaction coordinates and are therefore typically associated with much larger barriers. The formation of an epoxide facilitates the escape of the O atom though the fullerene cage (Fig 5d), with the energy barrier for the O atom penetrating through C_{60} *via* an epoxide intermediate calculated as 3.56 eV (for comparison, the barrier for penetration through graphene is 5.5 eV[41]). The O atom remains bonded to two carbon atoms of C_{60} during the emission process, effectively pushing through a C-C bond (Fig 5c). In contrast, the pathways for fluorine escape are limited: the F atom requires a greater distortion of the fullerene cage during emission than an O atom. This results in a much higher energy barrier of 8.87 eV, consistent with the higher stability of the molecules we observed in TEM for $(HF@C_{60})@SWNT$, with some fullerene cages persisting virtually unchanged up to doses of ~ $2 \cdot 10^9$ e^- nm^{-2} (Fig 1e). Therefore, the observed lower stability of $O@C_{60}$ is due to a combination of the lower barrier for escape of the O atom from C_{60} coupled with a higher energy available to be transferred from the e-beam to O atom *via* H atoms. Overall, the escape of oxygen from C_{60} has a drastic impact on the integrity and reactivity of the fullerene cage (unlike the escape of hydrogen), with the highly reactive epoxide group able to cross-link, dimerise and polymerise the molecules, similar to a polymerisation process of fullerene epoxide in $C_{60}O$ in nanotubes described in our earlier work.[42] Taken together, these considerations explain the fast onset of cross-linking and oligomerisation we observe for $(H_2O@C_{60})@SWNT$ under electron irradiation (Fig 1d), compared to the relative stability of $(HF@C_{60})@SWNT$ at similar electron doses following the emission of hydrogen (Fig 1e).

CONCLUSIONS

In summary, results of our experimental measurements and theoretical modelling indicate that kinetic energy transferred directly from the electron beam to hydrogen atoms of small molecules, HF or H_2O, encapsulated in fullerene cages C_{60} causes a homolytic dissociation of X-H bonds (where X is F or O). Hydrogen atoms activated by the electron beam are expelled through the C_{60} cage, leaving charge neutral F or O atoms within the fullerene. Fast hydrogen atoms knocked out from small molecules by the e-beam have a significant impact on the surrounding atoms by transferring their kinetic energy to other atoms (O, F or C) and stimulating transformations in molecules which otherwise would not take place. In essence, the hydrogen atoms can amplify the impact of the e-beam on other atoms by a factor of ~3.4-3.8 (depending on the atomic mass of the atom receiving impact), which may have important implications for TEM analysis of organic or hydrated materials, including cryo-TEM of biological molecules frozen in a film of ice, although it should be noted that in such samples electron-electron damage mechanisms tend to dominate. Surprisingly, $F@C_{60}$ formed in the e-beam appears to be a significantly more stable molecule, as compared to $O@C_{60}$ formed from $H_2O@C_{60}$ under analogous conditions. This suggests the fundamental feasibility of the entrapment of atomic fluorine within C_{60}, similar to $N@C_{60}$.[43–46]

METHODS

Materials preparation. Endohedral fullerenes HF@C_{60} and H_2O@C_{60} were synthesised and isolated by previously reported methods, references 26 and 28 respectively. The molecules were inserted into nanotubes through sublimation at 500 °C in vacuum, and the (HF@C_{60})@SWNT and (H_2O@C_{60})@SWNT samples dispersed onto lacey carbon Cu TEM grids by drop casting suspensions in isopropanol. Crystals of HF@C_{60} were deposited onto TEM grids using the same method.

Image and spectrum acquisition. HRTEM investigations were carried out using a dedicated low voltage microscope – the SALVE (sub-Ångström low voltage electron microscopy) instrument based on a Thermo Fischer Themis[3] platform equipped with a dedicated chromatic and spherical (C_c/C_s) aberration corrector developed by CEOS. The SALVE instrument is fully corrected for the 5th order axial geometric aberrations (including C_S and C_5), 3rd order off-axial geometric aberrations, and the for the 1st order chromatic aberrations (C_C).[47] The TEM was operated at 30 kV. Images with exposure times (0.2 to 2.0 seconds were acquired using a CETA 16 camera (using binning 2, resulting in images sized of 2048 by 2048 pixels). For all experiments were the dose rates in the order between $1 \cdot 10^6$ e^- nm^{-2} s^{-1} to $1 \cdot 10^7$ e^- nm^{-2} s^{-1}.

Additional scanning transmission electron microscopy (STEM) observations were carried out at 60 kV acceleration voltage on a monochromated Nion UltraSTEM 100MC 'Hermes' at the SuperSTEM laboratory. This microscope is equipped with a 5th order probe aberration corrector enabling a probe size of approximately 0.09 nm at 60 kV with a convergence semi-angle of 31 mrad in the conditions used for these experiments. The monochromator improves the native 350 meV energy resolution of the cold field emitter of this instrument to approximately 15 meV in practical experimental conditions (as estimated from the zero-loss-peak, ZLP, full width at half-maximum), with no loss of spatial resolution, enabling the acquisition of molecular vibrational signals. The use of a higher beam energy (60 keV) compared to the HRTEM experiments was necessary to retain both high spatial and energy resolution (at 30 keV in the current configuration of the instrument used, the spatial resolution would not have been sufficient to distinguish the atomic contrast of the object). The beam current with the monochromator slit fully open was approximately 80 pA, reduced to approximately 5 pA when the slit is closed for high energy resolution work, also resulting in significantly reduced dose-rates (specified within the main text). High-angle annular-dark-field images were recorded using a detector with a semi-angular range of 85-195 mrad. Electron energy loss spectra were acquired on a Gatan Enfinium ERS spectrometer, modified with high stability electronics for improved resolution. The EELS collection semi-angle was 36 mrad, with spectra acquired in 'dual-EELS' mode whereby two spectra are recorded quasi simultaneously: one with extremely short exposure time (typically 0.001 s) contains the full zero loss and is used for energy calibration, while the other is optimised for higher signal-to-noise ratio with longer acquisition times (0.15 s for the spectra shown in Fig 3e) with the zero-loss peak shifted off the camera to avoid saturation. Spectra in aloof geometry were averaged from a large 'spectrum image' (whereby the probe is scanned across a defined region of interest, and the EELS and imaging signal acquired at each probe position), after careful energy re-alignment and calibration using the low loss information from the dual-EELS pair. The three spectra were extracted from the same region in the spectrum images with the same number of pixels in order to keep the total electron doses comparable. The ZLPs were removed from experimental spectra using two-term exponential functions on a window below 0.12 eV, preceding the first observable spectral feature of interest, using scripts written in MATLAB.[48] STEM images shown in Fig 3a,c were processed using a "difference of Gaussians" filter,[49] see Supporting Information S11 for original unprocessed images. Finally, fingerprinting of the single F atoms using EELS spectrum imaging was carried out on a non-monochromated Nion UltraSTEM100 microscope, operated at 60 kV. This microscope is equipped with a Gatan Enfina EELS spectrometer: the EELS collection aperture semi-angle was 36 mrad as above, with similar electron optical parameters and probe size and currents as above; the energy dispersion was 0.4 eV/channel, allowing the simultaneous detection of the C *K* (284 eV onset) and F *K* (685 eV onset) ionisation edges. A pixel dwell time of 0.6 s and pixel sizes varying between 0.1 nm and 0.15 nm (0.12 nm in the data presented in Fig 4) were chosen as a compromise between the low signal levels due to the small inelastic scattering cross-section of F and the increased dose inevitably resulting in heavy e-beam damage to a number of the C_{60} molecular cages. The maps presented in Fig 4 were generated by integrating the F and C signals over a 50 eV window above their respective K ionisation edge onsets after background subtraction using a standard power law model. No other processing was applied.

Image calculations. Atomic models of nanotubes including C_{60} molecules and HF molecules were built using a custom-made program. Transmission electron microscopy image simulation was carried out using the multi-slice program QSTEM [www.qstem.org] with a fixed number of 30 slices per tube (which corresponds to an average slice thickness of 0.05 nm). Images with a total size of 512 × 512 pixels and identical sampling as in the experiment were calculated. Parameters of the geometric aberrations including the 3rd order spherical aberrations C_S and the 5th order spherical aberrations C_5 were set for optimum black resp. white atoms contrast. The focus was chosen around Scherzer focus to match the experiments. The dampening of the contrast transfer function (CTF) includes a focus spread (standard deviation) $\sigma_{\Delta f}$ of 0.5 nm which corresponds to the remaining residual focus spread caused by higher orders of the chromatic aberrations. The dampening effect of the images spread[50] which is an intrinsic property of C_C correctors was set to 25 pm. The dampening of the contrast because of the camera was included by adding the corresponding modulation transfer function (MTF) to the simulated images. The MTF of the camera were prior measured using single pixel illumination.[51] The effect of limited electron dose was emulated by applying noise to the calculated images using a custom-made Monte-Carlo program exploiting the Poisson statistics of electrons. HAADF-STEM image simulations were carried using atomic models optimised in LAMMPS using a version of the ReaxFF forcefield parameterised for carbon, fluorine and hydrogen atoms,[52] using the Dr Probe multi-slice program: the probe convergence and detector angular range reflected experimental values, with optical aberrations set to 0 for simplicity.[53] As with TEM simulations, a number of 30 slices per tube was chosen, with 512 × 512 pixel simulation size and sampling carefully selected to match the chosen detector range. A total of 30 frozen phonon configurations was calculated to simulate the effect of thermal diffuse scattering, and a Gaussian convolution was applied to the final image to reflect the estimated 0.5 Å source size (partial coherence effect).

Density functional theory calculations. Density functional theory (DFT) calculations were performed using the Q-Chem 5.0 quantum chemistry software package,[54] using the dispersion corrected range separated hybrid ωB97X-D exchange-correlation functional[55] and a 6-311G* basis set.

The potential energy curves in Fig 5a,b were calculated at this level of theory with a series of unrestricted single point energy calculations as a function of H-F bond length. As the exceptionally high velocity of energetic hydrogen atoms results in atom emission on very quick timescales relative to thermal vibrations (several femtoseconds), the other atoms in the system are essentially stationary and the hydrogen atom will experience the potential energy landscape shown in Fig 5b, which represents the lengthening of the H-F interatomic distance through the centre of a fullerene hexagon without optimisation of the rest of the system. The difference in energy between homolytic and heterolytic bond dissociation of HF was calculated as the difference in energy of $E(H^0)+E(F^0)$ (homolytic) and $E(H^+)+E(F^-)$ (heterolytic). The energy difference for dissociation of H_2O was calculated as the difference in energy between $E(HO^0)+E(H^0)$ (homolytic) and $E(HO^-)+E(H^+)$ (heterolytic) for removal of one hydrogen, and between $E(O^0)+2E(H^0)$ (homolytic) and $E(O^{2-})+2E(H^+)$ (heterolytic) for removal of both hydrogen atoms.

Born-Oppenheimer molecular dynamics simulations at this level of theory were used to model electron impacts, by adding the velocity transferred by the incident electron to the primary knock-on atom at a single time-step of the simulation (reflecting the extremely quick interaction with the relativistic electron). Initial atomic velocities were generated from a Maxwell-Boltzmann distribution at 298 K. A Fock matrix extrapolation procedure with a sixth-order polynomial and 12 Fock matrices was used in order to lower computational cost by using information from previous time-steps to accelerate SCF convergence times.[56] The SCF convergence criterion was 10^{-6} and the threshold for neglect of two electron integrals was 10^{-9} E_h. A 0.5 fs time-step was generally used, except in simulations involving highly energetic hydrogen atoms, in which case 0.05 fs was used to ensure conservation of energy. Electron impacts modelling the emission of F and O atoms from the fullerene were performed at transferred energies corresponding to E_{Tmax} and E_{Tmax}^{H} at 30 keV. For HF, atomic F, and H_2O, each kinetic energy was transferred in five high symmetry directions: towards a carbon atom, towards the centre of the [5,6] and [6,6] bonds, and towards the centre of a hexagon and pentagon. For the endo-epoxide, each kinetic energy was transferred towards the centre of the corresponding C-C bond for an epoxide on each of the [5,6] and [6,6] C-C bonds, and to carbon atoms in six high symmetry directions: two perpendicular to C-C, two parallel to O-C, and two relative to the fullerene hexagon. The threshold energy for inversion of the endohedral to exohedral epoxide was calculated by reducing the initial transferred energy in steps of 0.1 eV to discover the lowest energy that would result in the formation of an exohedral epoxide species.

For calculations of transition state structures and energy barriers, approximate reaction paths and transition states were found with the freezing string method,[57] using a quasi-Newton line search method with approximate Hessians updated by the Broyden-Fletcher-Goldfarb-Shanno method (FSM-BFGS).[58] The transition state was then optimised with the partitioned rational-function optimization (P-RFO) algorithm[58] using the approximate Hessian, and confirmed with a finite difference Davidson method.[59] For this level of theory, the mean absolute error is below 0.07 eV (against a test set of the NHTBH38/04 database of non-hydrogen transfer barrier heights).[55,60]

ACKNOWLEDGEMENTS

We gratefully acknowledge Dr. Anna Carlsson (Thermofisher Scientifc Nanoport, Eindhoven, NL) for supporting initial 30 kV STEM experiments. We acknowledge support of the Nanoscale & Microscale Research Centre (nmRC) and Centre for Sustainable Chemistry (CSC) University of Nottingham. S. Skowron and E. Besley are grateful to the High Performance Computing (HPC) Facility at the University of Nottingham for providing computational time. J. Biskupek and U. Kaiser gratefully acknowledge the support of the "Graphene Flagship" and DFG SPP "Graphene" as well as the DFG and the Ministry of Science, Research and the Arts (MWK) of Baden-Wuerttemberg within the frame of the SALVE (Sub Angstrom Low Voltage Electron microscopy) project. SuperSTEM is the EPSRC National Research Facility for Advanced Electron Microscopy. A. Khlobystov, S. Alom, K. Fung, R. Whitby and M. Levitt acknowledge support from the Engineering and

Physical Science Research Council (EPSRC; grant numbers EP/M001962/1, EP/P009980/1 and EP/L022494/1).

Supporting Information Available:

C_{60} molecules without any filling; Contrast of F-atoms within C_{60}; Extended irradiation of HF@C_{60} during EDXS acquisition; Calculated geometry of HF@C_{60} and H_2O@C_{60}; Reaction paths of oxygen emission from fullerene; Predicted dose for hydrogen emission from HF@C_{60}; HRTEM image simulation: (HF@C_{60})@SWNT; HRTEM image simulation: (H2O@C_{60})@SWNT; Comparison of reaction rates at 30 and 80 keV; Hindered rotation of HF@C_{60} in SWNT; Unfiltered 60 kV STEM images of (HF@C_{60})@SWNT; HRTEM average contrast analysis; 30 kV STEM images of (HF@C_{60})@SWNT.

Video 1. HRTEM imaging of dynamics of (HF@C_{60})@SWNT using 30 keV e-beam.

Video 2. HRTEM imaging of dynamics of (H_2O@C_{60})@SWNT using 30 keV e-beam.

Video 3a,3b. HRTEM imaging of dynamics of (HF@C_{60})@SWNT using 80 keV e-beam.

Video 4. HRTEM imaging of dynamics of (H_2O@C_{60})@SWNT using 80 keV e-beam.

Video 5. HRTEM imaging of dynamics of C_{60}@SWNT using 30 keV e-beam.

Video 6. Homolytic bond dissociation of HF.

Video 7. DFT-MD trajectories of HF@C_{60} following electron impacts on hydrogen.

Video 8. DFT-MD trajectory of emission of an oxygen atom from the endohedral epoxide.

Supporting Coordinates. Atomic coordinates for stationary point structures.

This material is available free of charge via the Internet at http://pubs.acs.org

REFERENCES

(1) Skowron, S. T.; Chamberlain, T. W.; Biskupek, J.; Kaiser, U.; Besley, E.; Khlobystov, A. N. Chemical Reactions of Molecules Promoted and Simultaneously Imaged by the Electron Beam in Transmission Electron Microscopy. *Acc. Chem. Res.* **2017**, *50*, 1797–1807.

(2) Allen, C. S.; Ito, Y.; Robertson, A. W.; Shinohara, H.; Warner, J. H. Two-Dimensional Coalescence Dynamics of Encapsulated Metallofullerenes in Carbon Nanotubes. *ACS Nano* **2011**, *5*, 10084–10089.

(3) Markevich, A.; Kurasch, S.; Lehtinen, O.; Reimer, O.; Feng, X.; Müllen, K.; Turchanin, A.; Khlobystov, A. N.; Kaiser, U.; Besley, E. Electron Beam Controlled Covalent Attachment of Small Organic Molecules to Graphene. *Nanoscale* **2016**, *8*, 2711–2719.

(4) Chamberlain, T. W.; Biskupek, J.; Skowron, S. T.; Markevich, A. V.; Kurasch, S.; Reimer, O.; Walker, K. E.; Rance, G. A.; Feng, X.; Müllen, K.; Turchanin, A.; Lebedeva, M. A.;

Majouga, A. G.; Nenajdenko, V. G.; Kaiser, U.; Besley, E.; Khlobystov, A. N. Stop-Frame Filming and Discovery of Reactions at the Single-Molecule Level by Transmission Electron Microscopy. *ACS Nano* **2017**, *11*, 2509–2520.

(5) Chamberlain, T. W.; Biskupek, J.; Skowron, S. T.; Bayliss, P. A.; Bichoutskaia, E.; Kaiser, U.; Khlobystov, A. N. Isotope Substitution Extends the Lifetime of Organic Molecules in Transmission Electron Microscopy. *Small* **2015**, *11*, 622–629.

(6) Skowron, S. T.; Lebedeva, I. V; Popov, A. M.; Bichoutskaia, E. Approaches to Modelling Irradiation-Induced Processes in Transmission Electron Microscopy. *Nanoscale* **2013**, *5*, 6677–6692.

(7) Khlobystov, A. N.; Porfyrakis, K.; Kanai, M.; Britz, D. A.; Ardavan, A.; Shinohara, H.; Dennis, T. J. S.; Briggs, G. A. D. Molecular Motion of Endohedral Fullerenes in Single-Walled Carbon Nanotubes. *Angew. Chemie Int. Ed.* **2004**, *43*, 1386–1389.

(8) Ran, K.; Zuo, J.-M.; Chen, Q.; Shi, Z. Electron Beam Stimulated Molecular Motions. *ACS Nano* **2011**, *5*, 3367–3372.

(9) Begtrup, G. E.; Gannett, W.; Yuzvinsky, T. D.; Crespi, V. H.; Zettl, A. Nanoscale Reversible Mass Transport for Archival Memory. *Nano Lett.* **2009**, *9*, 1835–1838.

(10) Zhao, J.; Huang, J.-Q.; Wei, F.; Zhu, J. Mass Transportation Mechanism in Electric-Biased Carbon Nanotubes. *Nano Lett.* **2010**, *10*, 4309–4315.

(11) Somada, H.; Hirahara, K.; Akita, S.; Nakayama, Y. A Molecular Linear Motor Consisting of Carbon Nanotubes. *Nano Lett.* **2009**, *9*, 62–65.

(12) Ueno, Y.; Somada, H.; Hirahara, K.; Nakayama, Y.; Akita, S. Molecular Dynamics Simulations for Molecular Linear Motor Inside Nanotube. *Jpn. J. Appl. Phys.* **2009**, *48*, 06FG03.

(13) Barreiro, A.; Rurali, R.; Hernandez, E. R.; Moser, J.; Pichler, T.; Forro, L.; Bachtold, A. Subnanometer Motion of Cargoes Driven by Thermal Gradients Along Carbon Nanotubes. *Science* **2008**, *320*, 775–778.

(14) de Juan, A.; Pouillon, Y.; Ruiz-González, L.; Torres-Pardo, A.; Casado, S.; Martín, N.; Rubio, Á.; Pérez, E. M. Mechanically Interlocked Single-Wall Carbon Nanotubes. *Angew. Chemie Int. Ed.* **2014**, *53*, 5394–5400.

(15) López-Moreno, A.; Nieto-Ortega, B.; Moffa, M.; de Juan, A.; Bernal, M. M.; Fernández-Blázquez, J. P.; Vilatela, J. J.; Pisignano, D.; Pérez, E. M. Threading through Macrocycles Enhances the Performance of Carbon Nanotubes as Polymer Fillers. *ACS Nano* **2016**, *10*, 8012–8018.

(16) Khlobystov, A. N.; Britz, D. A.; Briggs, G. A. D. Molecules in Carbon Nanotubes. *Acc. Chem. Res.* **2005**, *38*, 901–909.

(17) Botos, A.; Biskupek, J.; Chamberlain, T. W.; Rance, G. A.; Stoppiello, C. T.; Sloan, J.; Liu,

Z.; Suenaga, K.; Kaiser, U.; Khlobystov, A. N. Carbon Nanotubes as Electrically Active Nanoreactors for Multi-Step Inorganic Synthesis: Sequential Transformations of Molecules to Nanoclusters and Nanoclusters to Nanoribbons. *J. Am. Chem. Soc.* **2016**, *138*, 8175–8183.

(18) Cao, K.; Skowron, S. T.; Biskupek, J.; Stoppiello, C. T.; Leist, C.; Besley, E.; Khlobystov, A. N.; Kaiser, U. Imaging an Unsupported Metal–Metal Bond in Dirhenium Molecules at the Atomic Scale. *Sci. Adv.* **2020**, *6*, eaay5849. https://doi.org/10.1126/sciadv.aay5849.

(19) Koshino, M.; Niimi, Y.; Nakamura, E.; Kataura, H.; Okazaki, T.; Suenaga, K.; Iijima, S. Analysis of the Reactivity and Selectivity of Fullerene Dimerization Reactions at the Atomic Level. *Nat. Chem.* **2010**, *2*, 117–124.

(20) Nakamura, E.; Harano, K. Chemical Kinetics Study through Observation of Individual Reaction Events with Atomic-Resolution Electron Microscopy. *Proc. Japan Acad. Ser. B* **2018**, *94*, 428–440.

(21) Levitt, M. H. Spectroscopy of Light-Molecule Endofullerenes. *Philos. Trans. R. Soc. A Math. Phys. Eng. Sci.* **2013**, *371*, 20120429–20120429.

(22) Beduz, C.; Carravetta, M.; Chen, J. Y.-C.; Concistre, M.; Denning, M.; Frunzi, M.; Horsewill, A. J.; Johannessen, O. G.; Lawler, R.; Lei, X.; Levitt, M. H.; Li, Y.; Mamone, S.; Murata, Y.; Nagel, U.; Nishida, T.; Ollivier, J.; Rols, S.; Room, T.; Sarkar, R.; *et al.*, Quantum Rotation of Ortho and Para-Water Encapsulated in a Fullerene Cage. *Proc. Natl. Acad. Sci.* **2012**, *109*, 12894–12898.

(23) Meier, B.; Mamone, S.; Concistrè, M.; Alonso-Valdesueiro, J.; Krachmalnicoff, A.; Whitby, R. J.; Levitt, M. H. Electrical Detection of Ortho–Para Conversion in Fullerene-Encapsulated Water. *Nat. Commun.* **2015**, *6*, 8112.

(24) Murata, M.; Murata, Y.; Komatsu, K. Synthesis and Properties of Endohedral C 60 Encapsulating Molecular Hydrogen. *J. Am. Chem. Soc.* **2006**, *128*, 8024–8033.

(25) Kurotobi, K.; Murata, Y. A Single Molecule of Water Encapsulated in Fullerene C60. *Science* **2011**, *333*, 613–616.

(26) Krachmalnicoff, A.; Bounds, R.; Mamone, S.; Alom, S.; Concistrè, M.; Meier, B.; Kouřil, K.; Light, M. E.; Johnson, M. R.; Rols, S.; Horsewill, A. J.; Shugai, A.; Nagel, U.; Rõõm, T.; Carravetta, M.; Levitt, M. H.; Whitby, R. J. The Dipolar Endofullerene HF@C60. *Nat. Chem.* **2016**, *8*, 953–957.

(27) Levitt, M. H.; Horsewill, A. J. Nanolaboratories: Physics and Chemistry of Small-Molecule Endofullerenes. *Philos. Trans. R. Soc. A Math. Phys. Eng. Sci.* **2013**, *371*, 20130124–20130124.

(28) Krachmalnicoff, A.; Levitt, M. H.; Whitby, R. J. An Optimised Scalable Synthesis of H 2 O@C 60 and a New Synthesis of H 2 @C 60. *Chem. Commun.* **2014**, *50*, 13037–13040.

(29) Ulbricht, H.; Moos, G.; Hertel, T. Interaction of C60 with Carbon Nanotubes and Graphite.

Phys. Rev. Lett. **2003**, *90*, 095501.

(30) Füller, T.; Banhart, F. *In Situ* Observation of the Formation and Stability of Single Fullerene Molecules under Electron Irradiation. *Chem. Phys. Lett.* **1996**, *254*, 372–378.

(31) Krivanek, O. L.; Lovejoy, T. C.; Dellby, N.; Aoki, T.; Carpenter, R. W.; Rez, P.; Soignard, E.; Zhu, J.; Batson, P. E.; Lagos, M. J.; Egerton, R. F.; Crozier, P. A. Vibrational Spectroscopy in the Electron Microscope. *Nature* **2014**, *514*, 209–212.

(32) Meyer, J. C.; Kurasch, S.; Park, H. J.; Skakalova, V.; Künzel, D.; Groß, A.; Chuvilin, A.; Algara-Siller, G.; Roth, S.; Iwasaki, T.; Starke, U.; Smet, J. H.; Kaiser, U. Experimental Analysis of Charge Redistribution Due to Chemical Bonding by High-Resolution Transmission Electron Microscopy. *Nat. Mater.* **2011**, *10*, 209–215.

(33) Abellan, P.; El-Khoury, P. Z.; Ramasse, Q. M. Mapping VIS-Terahertz (≤17 THz) Surface Plasmons Sustained on Native and Chemically Functionalized Percolated Gold Thin Films Using EELS. *Microscopy* **2018**, *67*, i30–i39.

(34) Egerton, R. F. Vibrational-Loss EELS and the Avoidance of Radiation Damage. *Ultramicroscopy* **2015**, *159*, 95–100.

(35) Krivanek, O. L.; Dellby, N.; Hachtel, J. A.; Idrobo, J.-C.; Hotz, M. T.; Plotkin-Swing, B.; Bacon, N. J.; Bleloch, A. L.; Corbin, G. J.; Hoffman, M. V.; Meyer, C. E.; Lovejoy, T. C. Progress in Ultrahigh Energy Resolution EELS. *Ultramicroscopy* **2019**, *203*, 60–67.

(36) Abou-Hamad, E.; Kim, Y.; Wågberg, T.; Boesch, D.; Aloni, S.; Zettl, A.; Rubio, A.; Luzzi, D. E.; Goze-Bac, C. Molecular Dynamics and Phase Transition in One-Dimensional Crystal of C 60 Encapsulated Inside Single Wall Carbon Nanotubes. *ACS Nano* **2009**, *3*, 3878–3883.

(37) Halverson, T.; Iouchtchenko, D.; Roy, P.-N. Quantifying Entanglement of Rotor Chains Using Basis Truncation: Application to Dipolar Endofullerene Peapods. *J. Chem. Phys.* **2018**, *148*, 074112.

(38) Skowron, S. T.; Roberts, S. L.; Khlobystov, A. N.; Besley, E. The Effects of Encapsulation on Damage to Molecules by Electron Radiation. *Micron* **2019**, *120*, 96–103.

(39) Vehviläinen, T. T.; Ganchenkova, M. G.; Oikkonen, L. E.; Nieminen, R. M. Hydrogen Interaction with Fullerenes: From C20 to Graphene. *Phys. Rev. B* **2011**, *84*, 085447.

(40) *Handbook of Chemistry & Physics*, 58th ed.; Weast, R. C., Ed.; CSR Press: Boca Raton, Florida, 1979.

(41) Tsetseris, L.; Pantelides, S. T. Graphene: An Impermeable or Selectively Permeable Membrane for Atomic Species? *Carbon* **2014**, *67*, 58–63.

(42) Britz, D. A.; Khlobystov, A. N.; Porfyrakis, K.; Ardavan, A.; Briggs, G. A. D. Chemical Reactions inside Single-Walled Carbon Nano Test-Tubes. *Chem. Commun.* **2005**, 37.

(43) Morton, J. J. L.; Tyryshkin, A. M.; Ardavan, A.; Porfyrakis, K.; Lyon, S. A.; Andrew D. Briggs, G. Electron Spin Relaxation of N@C60 in CS2. *J. Chem. Phys.* **2006**, *124*, 014508.

(44) Zhou, S.; Rašović, I.; Briggs, G. A. D.; Porfyrakis, K. Synthesis of the First Completely Spin-Compatible N@C60 Cyclopropane Derivatives by Carefully Tuning the DBU Base Catalyst. *Chem. Commun.* **2015**, *51*, 7096–7099.

(45) Almeida Murphy, T.; Pawlik, T.; Weidinger, A.; Höhne, M.; Alcala, R.; Spaeth, J.-M. Observation of Atomlike Nitrogen in Nitrogen-Implanted Solid C60. *Phys. Rev. Lett.* **1996**, *77*, 1075–1078.

(46) Knapp, C.; Dinse, K.-P.; Pietzak, B.; Waiblinger, M.; Weidinger, A. Fourier Transform EPR Study of N@C60 in Solution. *Chem. Phys. Lett.* **1997**, *272*, 433–437.

(47) Linck, M.; Hartel, P.; Uhlemann, S.; Kahl, F.; Müller, H.; Zach, J.; Haider, M.; Niestadt, M.; Bischoff, M.; Biskupek, J.; Lee, Z.; Lehnert, T.; Börrnert, F.; Rose, H.; Kaiser, U. Chromatic Aberration Correction for Atomic Resolution TEM Imaging from 20 to 80 KV. *Phys. Rev. Lett.* **2016**, *117*, 076101.

(48) Fung, K. L. Y.; Fay, M. W.; Collins, S. M.; Kepaptsoglou, D. M.; Skowron, S. T.; Ramasse, Q. M.; Khlobystov, A. N. Accurate EELS Background Subtraction – an Adaptable Method in MATLAB. *Ultramicroscopy* **2020**, *217*, 113052.

(49) Krivanek, O. L.; Zhou, W.; Chisholm, M. F.; Idrobo, J. C.; Lovejoy, T. C.; Ramasse, Q. M.; Dellby, N. Gentle STEM of Single Atoms: Low KeV Imaging and Analysis at Ultimate Detection Limits. In *Low Voltage Electron Microscopy*; John Wiley & Sons, Ltd: Chichester, UK, 2012; pp 119–161.

(50) Uhlemann, S.; Müller, H.; Hartel, P.; Zach, J.; Haider, M. Thermal Magnetic Field Noise Limits Resolution in Transmission Electron Microscopy. *Phys. Rev. Lett.* **2013**, *111*, 046101.

(51) Lubk, A.; Röder, F.; Niermann, T.; Gatel, C.; Joulie, S.; Houdellier, F.; Magén, C.; Hÿtch, M. J. A New Linear Transfer Theory and Characterization Method for Image Detectors. Part II: Experiment. *Ultramicroscopy* **2012**, *115*, 78–87.

(52) Singh, S. K.; Srinivasan, S. G.; Neek-Amal, M.; Costamagna, S.; van Duin, A. C. T.; Peeters, F. M. Thermal Properties of Fluorinated Graphene. *Phys. Rev. B* **2013**, *87*, 104114.

(53) Barthel, J. Dr. Probe: A Software for High-Resolution STEM Image Simulation. *Ultramicroscopy* **2018**, *193*, 1–11.

(54) Shao, Y.; Gan, Z.; Epifanovsky, E.; Gilbert, A. T. B.; Wormit, M.; Kussmann, J.; Lange, A. W.; Behn, A.; Deng, J.; Feng, X.; Ghosh, D.; Goldey, M.; Horn, P. R.; Jacobson, L. D.; Kaliman, I.; Khaliullin, R. Z.; Kuś, T.; Landau, A.; Liu, J.; Proynov, E. I.; Rhee, Y. M.; *et al.*, M. Advances in Molecular Quantum Chemistry Contained in the Q-Chem 4 Program Package. *Mol. Phys.* **2015**, *113*, 184–215.

(55) Chai, J.-D.; Head-Gordon, M. Long-Range Corrected Hybrid Density Functionals with Damped Atom–Atom Dispersion Corrections. *Phys. Chem. Chem. Phys.* **2008**, *10*, 6615.

(56) Herbert, J. M.; Head-Gordon, M. Accelerated, Energy-Conserving Born–Oppenheimer Molecular Dynamics *via* Fock Matrix Extrapolation. *Phys. Chem. Chem. Phys.* **2005**, *7*,

3269.

(57) Behn, A.; Zimmerman, P. M.; Bell, A. T.; Head-Gordon, M. Efficient Exploration of Reaction Paths *via* a Freezing String Method. *J. Chem. Phys.* **2011**, *135*, 224108.

(58) Mallikarjun Sharada, S.; Zimmerman, P. M.; Bell, A. T.; Head-Gordon, M. Automated Transition State Searches without Evaluating the Hessian. *J. Chem. Theory Comput.* **2012**, *8*, 5166–5174.

(59) Sharada, S. M.; Bell, A. T.; Head-Gordon, M. A Finite Difference Davidson Procedure to Sidestep Full *Ab Initio* Hessian Calculation: Application to Characterization of Stationary Points and Transition State Searches. *J. Chem. Phys.* **2014**, *140*, 164115.

(60) Zhao, Y.; Lynch, B. J.; Truhlar, D. G. Development and Assessment of a New Hybrid Density Functional Model for Thermochemical Kinetics. *J. Phys. Chem. A* **2004**, *108*, 2715–2719.

For Table of Contents Only: